New Journal of Physics
The open access journal for physics

Flux lattices reformulated

G Juzeliūnas[1,3] and I B Spielman[2,3]

[1] Institute of Theoretical Physics and Astronomy, Vilnius University, A Goštauto 12, Vilnius LT-01108, Lithuania
[2] Joint Quantum Institute, National Institute of Standards and Technology, and University of Maryland, Gaithersburg, MD 20899, USA
E-mail: Gediminas.Juzeliunas@tfai.vu.lt and ian.spielman@nist.gov

New Journal of Physics **14** (2012) 123022 (22pp)
Received 11 July 2012
Published 12 December 2012
Online at http://www.njp.org/
doi:10.1088/1367-2630/14/12/123022

Abstract. We theoretically explore the optical flux lattices produced for ultra-cold atoms subject to laser fields where both the atom–light coupling and the effective detuning are spatially periodic. We analyze the geometric vector potential and the magnetic flux it generates, as well as the accompanying geometric scalar potential. We show how to understand the gauge-dependent Aharonov–Bohm singularities in the vector potential, and calculate the continuous magnetic flux through the elementary cell in terms of these singularities. The analysis is illustrated with a square optical flux lattice. We conclude with an explicit laser configuration yielding such a lattice using a set of five properly chosen beams with two counterpropagating pairs (one along the x axes and the other along the y axes), together with a single beam along the z-axis. We show that this lattice is not phase-stable, and identify the one phase-difference that affects the magnetic flux. Thus armed with a realistic laser setup, we directly compute the Chern number of the lowest Bloch band to identify the region where the non-zero magnetic flux produces a topologically non-trivial band structure.

[3] Authors to whom any correspondence should be addressed.

Contents

1. Introduction

Atomic quantum gases are systems where condensed matter and atomic physics meet. Cold atomic gases exhibit a number of condensed matter phenomena [1–4], such as the superfluid–Mott transition [5], Berezinskii–Kosterlitz–Thouless superfluidity [6] and the Bose–Einstein condensation-to-Bardeen–Cooper–Schrieffer crossover [7, 8]. Because the atoms constituting these quantum gases are electrically neutral, no vector potentials affect their center-of-mass motion. Such vector potentials might provide the Lorentz force essential for magnetic phenomena in solids, such as the quantum Hall effect [9]. The standard way to produce an artificial magnetic field is to rotate an atomic cloud, leading to a non-trivial vector potential in the rotating frame of reference [10, 11]. The various proposed schemes to create an effective magnetic field for ultra-cold atoms without rotation [12] can be divided into two categories.

The first category relies on a primary optical lattice which traps atoms at its sites. The magnetic flux is created by inducing asymmetric tunneling between lattice sites, so that atoms acquire a non-zero phase after completing a closed loop along a plaquette [13–22]. Such asymmetries can be induced by laser-assisted tunneling [13–16, 18, 21, 23] or using time-dependent lattices [15, 17, 19, 20, 22].

The second group of proposals is based on the concept of geometric gauge potentials which are encountered in many areas of physics [24–32]. In atomic gases, the geometric vector and scalar potentials were first considered in the late 1990s for atoms interacting with the laser fields [33–35], where the atoms are ‘dressed’ by laser beams. The resulting position dependence of the dressed internal states leads to geometric vector and scalar potentials. The method can provide a non-zero effective magnetic field using non-trivial spatial arrangements of laser fields [36–43] or position-dependent detuning of the atom–light coupling [44–46].

In these approaches the magnetic flux through the atomic cloud scales linearly with the cloud's extent [40, 42, 44, 45] and not its area. For large systems this is a major obstacle to reaching the sizable magnetic fluxes required for achieving the fractional Hall effect [47].

A new class of geometric potentials termed 'flux lattices' were recently shown to yield a magnetic flux proportional to the surface area of the atomic cloud [48], see also [49]. In this proposal, a two-level atom was coupled to a spatially periodic laser field where both the atom–light coupling and the detuning term were oscillatory. This approach simultaneously generates a non-staggered magnetic flux along with a lattice potential, thus providing an optical flux lattice [48].

The vector potential $\mathbf{A}$ plays an important role in the quantum physics [50]. It is featured in the Peierls substitution [51–53] widely used in tight binding models in solids to describe the motion of charged particles in a magnetic field. Specifically, the tunneling matrix element between the lattice sites $\mathbf{r}_A$ and $\mathbf{r}_B$ acquires the Peierls phase factor proportional to $\int_{\mathbf{r}_A}^{\mathbf{r}_B} \mathbf{A} \cdot \mathrm{d}\mathbf{r}$. Similar Peierls phase factors emerge also in the tunneling matrix elements between the sites of an optical lattice for electrically neutral ultra-cold atoms affected by an artificial magnetic field.

The geometric vector potential contains gauge-dependent singularities for optical flux lattices: to avoid these singularities, Cooper [48] concentrated on the magnetic flux rather than on the underlying vector potential. Here we explicitly reformulate the previous analysis of the optical flux lattices and explore them directly in terms of the geometric vector potential, as well as an accompanying geometric scalar potential. We show how to understand the gauge-dependent Aharonov–Bohm (AB) singularities [50] appearing in the vector potential and calculate the continuous magnetic flux through the elementary cell in terms of these singularities, providing a straightforward method of finding the total magnetic flux. Our analysis is not restricted to two atomic internal states and is applicable to situations where the atom in the external electromagnetic field has total spin-f (with $2f+1$ internal atomic states). This is important for applying the theory to the specific atomic setups which involve more than two atomic internal states. For instance, the $f = 1$ and 2 situations directly describe the two hyperfine manifolds in ^{87}Rb's ground electronic state.

Next, we analyze a square optical flux lattice and describe a way of creating it using Raman coupling between the atomic magnetic sublevels. A related setup proposed recently by Cooper and Dalibard aimed at producing triangular and hexagonal optical flux lattices used three coplanar lasers intersecting at 120°, with an additional beam normal to the plane spanned by the first three [54]. Now we present an explicit laser configuration yielding a square flux lattice and directly compute the Chern number of the lowest Bloch band. We identify the region where the non-zero magnetic flux produces a topologically non-trivial band structure for this lattice. In this configuration, a non-zero and quantized geometric magnetic flux always traverses each unit cell; however, the band structure has non-zero Chern number only over a modest range of parameters. Because of this, we studied typical experimental imperfections, such as polarization errors or a possible phase mismatch of the lasers producing the flux lattice, and identified the factors that must be cared for in experiment.

2. Hamiltonian and its eigenstates

Before focusing on a specific physical system, we begin by considering the very general problem of a multi-level atom moving in the presence of a spatially inhomogenous coupling Hamiltonian (for example, produced by a combination of optical and magnetic fields). The Hamiltonian

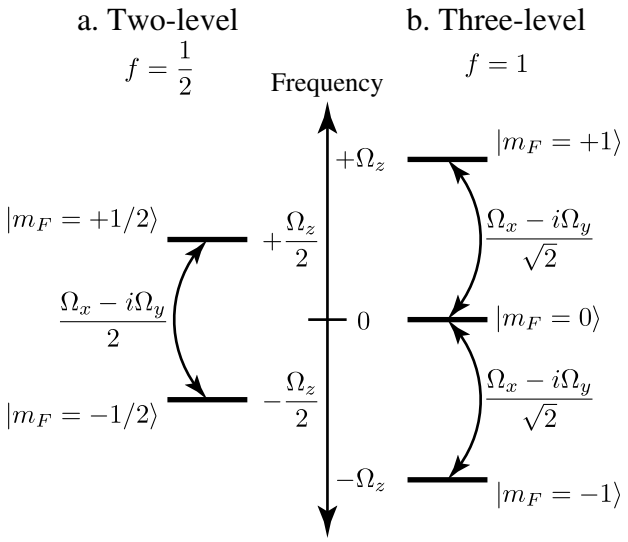

Figure 1. Traditional representation of the $\hat{M} = \boldsymbol{\Omega} \cdot \hat{\boldsymbol{F}}$ coupling scheme for (a) total angular momentum $f = 1/2$ and (b) total angular momentum $f = 1$. The bare atomic states are labeled by $|m_F\rangle$ and in both cases are detuned from each other by a frequency Ω_z. These levels are coupled with strength proportional to $\Omega_x \pm \mathrm{i}\,\Omega_y$.

describing such combined internal and center-of-mass motion is

$$\hat{H} = \left[\frac{\mathbf{p}^2}{2m} + U(\mathbf{r})\right]\hat{1} + \hat{M}(\mathbf{r}), \tag{1}$$

where $\mathbf{p} = -\mathrm{i}\,\hbar\nabla$ is the atomic momentum; $\hat{1}$ is the identity operator; $U(\mathbf{r})$ is a state-independent 'scalar' potential and $\hat{M}$ is the state-dependent part of the Hamiltonian. Here we focus on the case where the atom affected by the light fields behaves like a spin in a magnetic field, so the state-dependent Hamiltonian $\hat{M}(\mathbf{r})$ is

$$\hat{M}(\mathbf{r}) = \boldsymbol{\Omega} \cdot \hat{\boldsymbol{F}} \equiv \Omega \hat{F}_{\boldsymbol{\Omega}}, \tag{2}$$

where the vector $\boldsymbol{\Omega} \equiv \boldsymbol{\Omega}(\mathbf{r}) = (\Omega_x(\mathbf{r}), \Omega_y(\mathbf{r}), \Omega_z(\mathbf{r}))$ describes the spatially dependent coupling between the atomic internal states, $\Omega(\mathbf{r}) = |\boldsymbol{\Omega}(\mathbf{r})|$ being the total coupling strength; $\hat{\boldsymbol{F}} = (\hat{F}_x, \hat{F}_y, \hat{F}_z)$ is a vector operator satisfying the angular momentum algebra (to be referred to as the spin operator); and $\hat{F}_{\boldsymbol{\Omega}} \equiv \hat{F}_{\boldsymbol{\Omega}(\mathbf{r})}$ is the spatially dependent projection of $\hat{\boldsymbol{F}}$ along $\boldsymbol{\Omega}$. The position dependence of the Hamiltonian $\hat{M}(\mathbf{r})$ therefore originates from the position-dependent atom–light interaction through the coupling vector $\boldsymbol{\Omega}(\mathbf{r})$: a rapidly varying effective magnetic field. The physical implementation of such a Hamiltonian—equivalent to the Zeeman effect for a spatially dependent magnetic field—will be discussed in section 5.

Figure 1(a) depicts the (quasi-)spin-1/2 case, where $\hbar\Omega_z$ is the light-induced detuning between the two internal atomic states $|m_F = \pm 1/2\rangle$, and $\hbar(\Omega_x \pm \mathrm{i}\,\Omega_y)/2$ is the transition matrix element coupling the two states together. In what follows, we do not restrict ourselves to the spin-1/2 case and consider N internal states $|m_F\rangle$, where $m_F \in \{-f,\ f+1,\ \ldots,\ f\}$, and the quantity $f = (N-1)/2$ is the total angular momentum quantum number. The spin-1 case depicted in figure 1(b), has $f = 1$ and $N = 3$. We emphasize that the atomic states

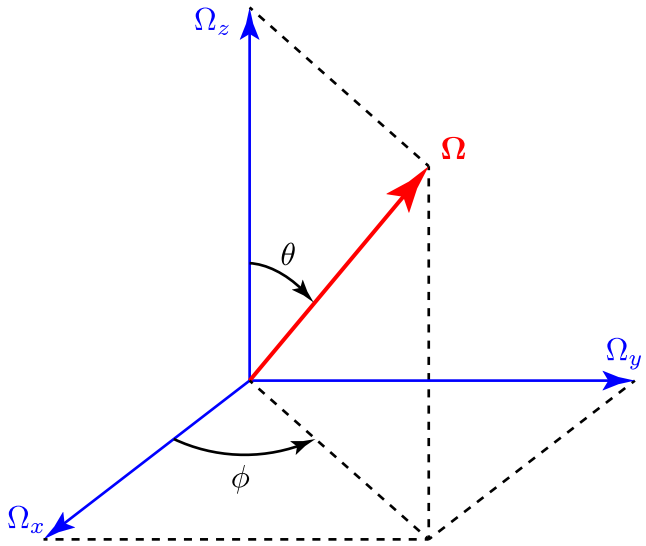

Figure 2. Representation of the coupling vector $\mathbf{\Omega} = (\Omega_x, \Omega_y, \Omega_z)$ in terms of the spherical angles θ and ϕ.

$|m_F\rangle$ do not necessarily represent the true spin states. They can be the atomic internal states of arbitrary origin, provided that the operator $\hat{F}$ featured in the atomic Hamiltonian obeys the angular momentum algebra.

2.1. Diagonalization via a unitary transformation

The projected momentum operator $\hat{F}_{\mathbf{\Omega}}$ entering the coupling Hamiltonian $\hat{M}$ can be related to the eigenstates of $\hat{F}_z$ via a unitary transformation $\hat{S}_{\mathbf{\Omega}}$ where

$$\hat{F}_{\mathbf{\Omega}} = \hat{S}_{\mathbf{\Omega}} \hat{F}_z \hat{S}_{\mathbf{\Omega}}^{-1}, \tag{3}$$

with

$$\hat{S}_{\mathbf{\Omega}} = \mathrm{e}^{-\mathrm{i}\,\hat{F}_z \phi/\hbar} \mathrm{e}^{-\mathrm{i}\,\hat{F}_y \theta/\hbar} \mathrm{e}^{\mathrm{i}\,\hat{F}_z \phi/\hbar}. \tag{4}$$

We parameterize the coupling vector $\mathbf{\Omega} = (\Omega_x, \Omega_y, \Omega_z)$ in terms of the spherical angles

$$\tan\phi = \frac{\Omega_y}{\Omega_x} \quad \text{and} \quad \cos\theta = \frac{\Omega_z}{\Omega} \tag{5}$$

shown in figure 2.

The operators $\hat{\mathbf{F}}^2$ and $\hat{F}_z$ have eigenstates $|m_F\rangle \equiv |f, m_F\rangle$ identified by the total angular momentum and its $\mathbf{e}_z$ projection

$$\hat{\mathbf{F}}^2 |m_F\rangle = \hbar^2 f(f+1) |m_F\rangle \quad \text{and} \quad \hat{F}_z |m_F\rangle = \hbar m_F |m_F\rangle,$$

f and m_F are the corresponding quantum numbers. Multiplying the last equation by $\hat{S}_{\mathbf{\Omega}}$, one has

$$\hat{F}_{\mathbf{\Omega}} |m_F, \mathbf{\Omega}\rangle = \hbar m_F |m_F, \mathbf{\Omega}\rangle, \quad \text{where } |m_F, \mathbf{\Omega}\rangle = \hat{S}_{\mathbf{\Omega}} |m_F\rangle. \tag{6}$$

The transformed states $|m_F, \mathbf{\Omega}\rangle$ are characterized by the projection $\hbar m_F$ of the momentum operator $\hat{\mathbf{F}}$ along the coupling vector $\mathbf{\Omega}$. In this way, the coupling Hamiltonian $\hat{M} = \Omega \hat{F}_{\mathbf{\Omega}}$ has a

set of position-dependent eigenstates $|m_F, \mathbf{\Omega}\rangle \equiv |m_F, \mathbf{\Omega}(\mathbf{r})\rangle$ related to the eigenstates of $\hat{F}_z$ via the position-dependent unitary transformation $\hat{S}_{\mathbf{\Omega}} \equiv \hat{S}_{\mathbf{\Omega}}(\mathbf{r})$. Using equation (4) for $\hat{S}_{\mathbf{\Omega}}$ and the fact that $|m_F\rangle$ is an eigenstate of $\hat{F}_z$, one arrives at the eigenstates

$$|m_F, \mathbf{\Omega}\rangle \equiv |m_F, \theta, \phi\rangle = \mathrm{e}^{\mathrm{i}(m_F - \hat{F}_z/\hbar)\phi} \mathrm{e}^{-\mathrm{i}\,\hat{F}_y\theta/\hbar}\, |m_F\rangle\,, \tag{7}$$

and energies

$$V_{m_F} = \hbar m_F \Omega \tag{8}$$

of the coupling Hamiltonian $\hat{M}$. Here, $V_{m_F} \equiv V(\mathbf{r})$ is the position-dependent energy of the local eigenstate $|m_F, \mathbf{\Omega}(\mathbf{r})\rangle$. Interestingly, similar kinds of eigenstates give rise to artificial gauge potential terms describing the rotation of diatomic molecules [26, 27] and the physics of atomic collisions [55, 56].

3. Gauge potentials

For an atom subject to the Hamiltonian of equation (1), the state vector describing both its internal and motional degrees of freedom can be expressed in the basis of dressed states

$$|\Psi(\mathbf{r}, t)\rangle = \sum_{m'_F} \psi_{m'_F}(\mathbf{r}, t)\, |m'_F, \mathbf{\Omega}\rangle\,,$$

where $\psi_{m'_F}(\mathbf{r}, t)$ is a wave function describing the atom's motion in the basis of local eigenstates $|m'_F, \mathbf{\Omega}\rangle \equiv |m'_F, \Omega(\mathbf{r})\rangle$. We are interested in the situation where $\Omega \neq 0$, so the local eigenstates $|m'_F, \mathbf{\Omega}\rangle$ are non-degenerate everywhere.

If an atom is prepared in one of these dressed states with $m'_F = m_F$, and its characteristic kinetic energy is small compared to $\Delta E = \hbar\Omega$ the energy difference between adjacent spin states, the internal state of the atom will adiabatically follow the dressed state $|m_F, \mathbf{\Omega}\rangle$ as the atom moves, and contributions from other states with $m'_F \neq m_F$ can be neglected. Projecting the full Schrödinger equation $\mathrm{i}\hbar\,|\dot{\Psi}(\mathbf{r}, t)\rangle = \hat{H}\,|\Psi(\mathbf{r}, t)\rangle$ onto the selected internal eigenstate $|m_F, \mathbf{\Omega}\rangle$ yields a reduced Schrödinger equation for the atomic center-of-mass motion $\mathrm{i}\hbar\dot{\psi}_{m_F}(\mathbf{r}, t) = H\psi_{m_F}(\mathbf{r}, t)$ with an effective Hamiltonian

$$H = \frac{[\mathbf{p} - \boldsymbol{\mathcal{A}}(\mathbf{r})]^2}{2m} + U(\mathbf{r}) + V(\mathbf{r}) + W(\mathbf{r}). \tag{9}$$

In this expression, the geometric vector

$$\boldsymbol{\mathcal{A}} \equiv \boldsymbol{\mathcal{A}}(\mathbf{r}) = \mathrm{i}\hbar\,\langle m_F, \mathbf{\Omega}|\,\nabla\,|m_F, \mathbf{\Omega}\rangle \tag{10}$$

and scalar

$$W \equiv W(\mathbf{r}) = \frac{\hbar^2}{2m} \sum_{m'_F \neq m_F} \left|\langle m'_F, \mathbf{\Omega}|\,\nabla\,|m_F, \mathbf{\Omega}\rangle\right|^2 \tag{11}$$

potentials appear due to the position dependence of the atomic dressed states. The vector potential can be interpreted as the average center-of-mass momentum of the selected internal state $|m_F\rangle \equiv |m_F(\mathbf{r})\rangle$. The scalar potential $W(\mathbf{r})$ emerges due to the elimination of the remaining atomic internal states. It represents the kinetic energy of the oscillatory micromotion [57, 58] due to the tiny transitions to the eliminated states $\left|m'_F, \mathbf{\Omega}\right\rangle \equiv \left|m'_F, \mathbf{\Omega}(\mathbf{r})\right\rangle$ with $m'_F \neq m_F$.

Equation (9) contains three distinct scalar potentials: (a) the state-independent potential $U(\mathbf{r})$ featured in the initial Hamiltonian (1), which we shall call $U(\mathbf{r})$ the 'scalar light shift'; (b) the 'adiabatic scalar potential' $V(\mathbf{r}) \equiv V_{m_F}$ arising from spatial variations in the magnitude $\Omega(\mathbf{r})$; and (c) the 'geometric scalar potential' $W(\mathbf{r})$ described above. All three contribute to the potential energy of atoms in the dressed state basis.

3.1. Vector and scalar potentials

Using equation (7), the matrix elements featured in the vector and scalar potentials are

$$\left\langle m'_F, \mathbf{\Omega}\right| \nabla \left| m_F, \mathbf{\Omega}\right\rangle = \frac{\mathrm{i}}{\hbar}\, \mathrm{e}^{\mathrm{i}(m_F - m'_F)\phi} \left\langle m'_F\right| \left[\left(\hbar m_F - \hat{\tilde{F}}_z\right) \nabla\phi - \hat{F}_y \nabla\theta\right] \left| m_F\right\rangle , \tag{12}$$

with $\hat{\tilde{F}}_z = \exp(\mathrm{i}\,\hat{F}_y\theta/\hbar)\,\hat{F}_z \exp(-\mathrm{i}\,\hat{F}_y\theta/\hbar) = \hat{F}_z\cos\theta + \hat{F}_x \sin\theta$. Using the identities $\langle m_F|\,\hat{F}_x\,|m_F\rangle = \langle m_F|\,\hat{F}_y\,|m_F\rangle = 0$ and $\langle m_F|\,\hat{F}_z\,|m_F\rangle = \hbar m_F$, equations (10)–(12) provide the vector potential

$$\mathcal{A}(\mathbf{r}) = \hbar m_F\,(\cos\theta - 1)\,\nabla\phi. \tag{13}$$

The vector potential (equation (13)) is maximum in magnitude when $m_F = \pm f$, and is zero for $m_F = 0$. For $f = 1/2$ and $m_F = 1/2$, equation (13) reduces to the result presented in [12].

To determine the scalar potential, we need the off-diagonal matrix elements of $\langle m'_F, \mathbf{\Omega}|\nabla|m_F, \mathbf{\Omega}\rangle$ which are

$$\left\langle m'_F, \mathbf{\Omega}\right| \nabla \left| m_F, \mathbf{\Omega}\right\rangle = -\frac{\mathrm{i}}{\hbar}\, \mathrm{e}^{\mathrm{i}(m_F - m'_F)\phi} \left\langle m'_F\right| \left(\hat{F}_x \sin\theta\nabla\phi + \hat{F}_y\nabla\theta\right) \left| m_F\right\rangle , \tag{14}$$

for $m'_F \neq m_F$. Combining equations (11) and (14), and using the completeness relation, we arrive at the geometric scalar potential

$$W(\mathbf{r}) = \frac{\hbar^2}{4m} g_{f,m_F} \left[\sin^2\theta\,(\nabla\phi)^2 + (\nabla\theta)^2\right], \tag{15}$$

with

$$g_{f,m_F} = f(f+1) - m_F^2. \tag{16}$$

We made use of $\langle m_F|\,\hat{F}_x^2\,|m_F\rangle = \langle m_F|\,\hat{F}_y^2\,|m_F\rangle = \hbar^2 g_{f,m_F}/2$. In particular, for $f = 1/2$, one has $g_{f,m_F} = 1/2$, and like the vector potential, the scalar potential reduces to that presented in [12]. Generally, $W(\mathbf{r})$ depends both on the total spin f and on its projection m_F. For instance, for $f = 1$, one has $g_{f,m_F} = 2 - m_F^2$, showing that $W(\mathbf{r})$ is maximum for $m_F = 0$ and is half of that for $m_F = \pm 1$.

3.2. Alternative gauge

Because each of the local eigenstates can be assigned an arbitrary position-dependent phase $\varphi_{m_F}(\mathbf{r})$, the vector potential $\mathcal{A}(\mathbf{r}) \equiv \mathcal{A}_{m_F}(\mathbf{r})$ in equation (13) is not unique. Effecting a state-dependent gauge transformation

$$|m_F, \mathbf{\Omega}\rangle' = \exp\left[\mathrm{i}\,\varphi_{m_F}(\mathbf{r})\right] |m_F, \mathbf{\Omega}\rangle , \tag{17}$$

the vector potential $\mathcal{A}(\mathbf{r})$ transforms to $\mathcal{A}'(\mathbf{r}) = \mathcal{A}(\mathbf{r}) - \hbar\nabla\varphi_{m_F}(\mathbf{r})$. For example, by taking $\varphi_{m_F}(\mathbf{r}) = -2\phi m_F$, the initial vector potential given by equation (13) becomes

$$\mathcal{A}'(\mathbf{r}) = \hbar m_F\,(\cos\theta + 1)\,\nabla\phi.$$

This seemingly esoteric change can have a significant impact because the $\nabla\phi$ contribution may be singular when $\cos\theta = \pm 1$ (near the z axes, see figure 2) if the factors $(\cos\theta - 1)$ or $(\cos\theta + 1)$ do not compensate for the singularity by simultaneously going to zero. The vector potential $\boldsymbol{\mathcal{A}}(\mathbf{r})$ is singular if $\theta = \pi$, but in the alternative gauge the vector potential $\boldsymbol{\mathcal{A}}'(\mathbf{r})$ has singularities when $\theta = 0$ *at spatially different points* than in the initial gauge! This is because the original and transformed local eigenstates ($|m_F, \boldsymbol{\Omega}\rangle \equiv |m_F, \theta, \phi\rangle$ and $|m_F, \boldsymbol{\Omega}\rangle' \equiv |m_F, \theta, \phi\rangle'$) do not have a well-defined phase for $\theta = \pi$ and 0, respectively.

3.3. Magnetic flux

The singularities in the vector potential correspond to AB-type flux tubes (piercing the $\mathbf{e}_x$–$\mathbf{e}_y$-plane) each with an integer flux quantum. Since the AB-type flux containing an integer number flux quanta cannot be observed [50], the two vector potentials $\boldsymbol{\mathcal{A}}(\mathbf{r})$ and $\boldsymbol{\mathcal{A}}'(\mathbf{r})$ are equivalent and produce the same effective magnetic field

$$\boldsymbol{\mathcal{B}}(\mathbf{r}) = \boldsymbol{\nabla} \times \boldsymbol{\mathcal{A}}(\mathbf{r}) = \hbar m_F \boldsymbol{\nabla} (\cos\theta) \times \boldsymbol{\nabla}\phi. \tag{18}$$

The gauge-dependent AB singularities (if any) present in the vector potential must be absent in equation (18) for $\boldsymbol{\mathcal{B}}(\mathbf{r})$.

It is convenient to represent the magnetic flux density in terms of the unit vector $\mathbf{N} = \boldsymbol{\Omega}/\Omega$

$$\boldsymbol{\mathcal{B}}(\mathbf{r}) = -\hbar m_F \frac{\nabla N_x \times \nabla N_y}{N_z}. \tag{19}$$

Thus if Ω_z alternates in sign at the points where $\Omega_x = \Omega_y = 0$, this might compensate the alternation of the $\nabla N_x \times \nabla N_y$ sign at these points, giving a non-zero magnetic flux, such as the one given by equation (30) below. This shows the necessity to have an oscillating detuning Ω_z in addition to the oscillating coupling $\Omega_x + \mathrm{i}\,\Omega_y$.

As we show in section 4.2, the geometric scalar potential $W(\mathbf{r})$ contributes most significantly to the overall scalar potential $U(\mathbf{r}) + V(\mathbf{r}) + W(\mathbf{r})$ at the maxima of the effective magnetic field where $\Omega_x + \mathrm{i}\,\Omega_y = 0$, and is zero at the points of the minimum magnetic flux where $\Omega_z = 0$.

3.4. Periodic atom–light coupling

Given this general background, we now consider the case where the coupling vector $\boldsymbol{\Omega} = (\Omega_x, \Omega_y, \Omega_z)$ is spatially periodic in the $\mathbf{e}_x$–$\mathbf{e}_y$-plane

$$\boldsymbol{\Omega}(\mathbf{r} + \mathbf{r}_{n,m}) = \boldsymbol{\Omega}(\mathbf{r}), \quad \mathbf{r}_{n,m} = n\mathbf{a}_1 + m\mathbf{a}_2, \tag{20}$$

where $\mathbf{a}_1$ and $\mathbf{a}_2$ are the primitive vectors defining a 2D lattice in the $\mathbf{e}_x$–$\mathbf{e}_y$-plane, with $\{n, m\} \in \mathbb{Z}$. In this case, both the atomic internal dressed states $|\tilde{m}_F(\mathbf{r})\rangle$ and the corresponding geometric potential $\boldsymbol{\mathcal{A}}(\mathbf{r})$ have the same periodicity (usually the geometric scalar potential $W(\mathbf{r})$ has a periodicity twice as small as the initial Hamiltonian and the geometric vector potential). Due to the periodicity of the vector potential the total flux over the elementary cell is zero:

$$\alpha = \frac{1}{\hbar}\oint_{\text{cell}} \boldsymbol{\mathcal{A}} \cdot \mathrm{d}\mathbf{r} = \frac{1}{\hbar}\iint_{\text{cell}} \boldsymbol{\mathcal{B}}_{\text{tot}} \cdot \mathrm{d}\mathbf{S} = 0, \tag{21}$$

where $\mathcal{B}_{\rm tot} = \mathcal{B}(\mathbf{r}) + \mathcal{B}_{\rm AB}(\mathbf{r})$ is the total magnetic flux density with contributions both from the continuous (background) magnetic flux density $\mathcal{B}(\mathbf{r})$ and possibly a set of gauge-dependent singular fluxes of the AB type represented by $\mathcal{B}_{\rm AB}(\mathbf{r})$.

Thus it is, strictly speaking, impossible to produce a non-zero effective magnetic flux α over the elementary cell using the periodic atom–light coupling. However, this does not preclude a non-staggered continuous magnetic flux density $\mathcal{B}(\mathbf{r})$ over the elementary cell as long as the vector potential contains (gauge-dependent) singularities of the AB type carrying together a non-zero number of the Dirac flux quanta. The AB singularities are associated with the points where the $\Omega_x + \mathrm{i}\,\Omega_y$ goes to zero and hence $\cos\theta \to \pm 1$. Deducting these non-measurable gauge-dependent singularities, the remaining flux over the elementary cell can be non-zero:

$$\alpha' = \frac{1}{\hbar}\iint_{\rm cell} \mathcal{B}\cdot \mathrm{d}\mathbf{S} = -\frac{1}{\hbar}\iint_{\rm cell} \mathcal{B}_{\rm AB}(\mathbf{r})\cdot \mathrm{d}\mathbf{S}\,. \tag{22}$$

The physical flux can hence be expressed in terms of the vector potential

$$\alpha' = -\frac{1}{\hbar}\sum \oint_{\rm singul} \mathcal{A}\cdot \mathrm{d}\mathbf{r} = -\frac{1}{\hbar}\sum \oint_{\rm singul} \mathcal{A}'\cdot \mathrm{d}\mathbf{r}, \tag{23}$$

where the summation is over the singular points of the vector potential (emerging at $\cos\theta \to -1$ for $\mathcal{A}$ and at $\cos\theta \to 1$ for $\mathcal{A}'$) around which the contour integration is carried out. In the neighborhood of each singular point (different for $\mathcal{A}$ and $\mathcal{A}'$) the vector potentials have a Dirac-string (the AB singularity) piercing the $\mathbf{e}_x$–$\mathbf{e}_y$-plane, giving

$$\mathcal{A} \to -2\hbar m_F \nabla\phi \quad \text{and} \quad \mathcal{A}' \to 2\hbar m_F \nabla\phi. \tag{24}$$

Thus each integral in equation (23) provides an integer number of the Dirac flux quanta. To obtain a non-zero flux α', the sum of the singular contributions must be non-zero. The flux is maximum if all these singular contributions have the same sign, as is the case for the square flux lattice considered below.

To summarize, the optical flux lattice contains a background non-staggered magnetic field $\mathcal{B}$ plus an array of gauge-dependent Dirac-string fluxes of opposite sign as compared to the background. The two types of fluxes compensate for each other, so the total magnetic flux over an elementary cell is zero as is required from the periodicity of the Hamiltonian. However, the Dirac-string fluxes are non-measurable and hence must be excluded from any physical consideration. As a result, a non-staggered magnetic flux over the optical flux lattice is possible.

4. Square optical flux lattice

We now construct a simple model flux lattice generated by a spatially periodic coupling vector $\mathbf{\Omega} = (\Omega_x, \Omega_y, \Omega_z)$ with components

$$\begin{aligned} \Omega_x &= \Omega_\perp \cos(x\pi/a), \\ \Omega_y &= \Omega_\perp \cos(y\pi/a), \\ \Omega_z &= \Omega_\parallel \sin(x\pi/a)\sin(y\pi/a). \end{aligned} \tag{25}$$

This coupling has period $2a$ along $\mathbf{e}_x$ and $\mathbf{e}_y$. It is convenient to define dimensionless coordinates $x' = \pi x/a$, $y' = \pi y/a$ and $z' = \pi z/a$. In the symmetric case, $\Omega_\perp = \Omega_\parallel$, the scheme reduces to the one considered previously in [48]. As will be discussed in section 5.1.2, the coupling vector

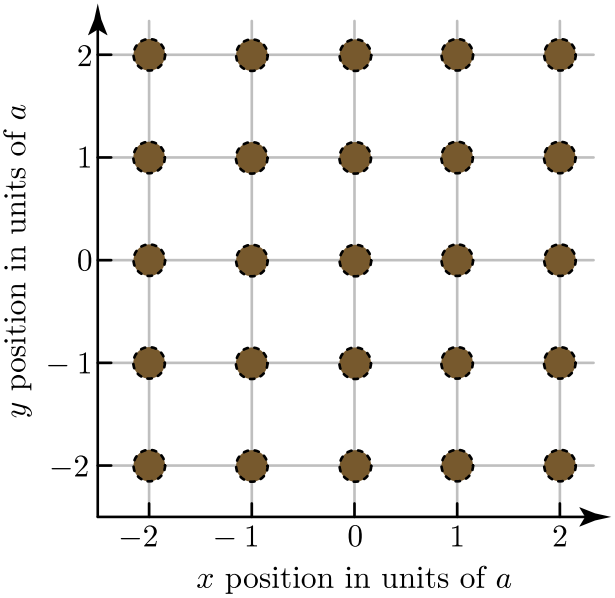

Figure 3. Sites of the square optical flux lattice corresponding to the minima of the adiabatic energy $V(x, y)$ for $m_F < 0$.

in equation (25) can be produced for alkali atoms using five laser beams intersecting at right angles: a pair counterpropagating along $\mathbf{e}_x$, a second pair counterpropagating along $\mathbf{e}_y$ and a single beam propagating along $\mathbf{e}_z$.

The total Rabi frequency resulting from equation (25) is

$$\Omega = \sqrt{\Omega_\parallel^2 + \left(\Omega_\perp^2 - \Omega_\parallel^2\right)\left(f_x^2 + f_y^2\right) + \Omega_\parallel^2 f_x^2 f_y^2}, \tag{26}$$

where $f_u = \cos(u')$. The resulting adiabatic energies $V_{m_F} = \hbar m_F \Omega$ have periodicity a, half that of the atom–light coupling.

When $\Omega_\perp^2 > \Omega_\parallel^2/2$, the minima of the $m_F < 0$ adiabatic scalar potential $V(x, y)$ are positioned at $x'_n = \pi n$ and $y'_m = \pi m$ (brown dots in figure 3) where $\Omega_z = 0$. The energy maxima are positioned at $x'_{n,\max} = \pi(n + 1/2)$ and $y'_{m,\max} = \pi(m + /2)$, where the atom–light coupling vanishes: $\Omega_x + \mathrm{i}\,\Omega_y \to 0$. Thus one has

$$\begin{aligned} E_{\min} &= V(\pi n, \pi m) = \hbar m_F \sqrt{2}\Omega_\perp, \\ E_{\max} &= V(\pi(n + 1/2), \pi(m + /2)) = \hbar m_F \Omega_\parallel. \end{aligned} \tag{27}$$

In the vicinity of the energy maxima, one has

$$\begin{aligned} \Omega_x &\approx -\Omega_\perp \left(x' - x'_{n,\max}\right)(-1)^n, \\ \Omega_y &\approx -\Omega_\perp \left(y' - y'_{m,\max}\right)(-1)^m, \\ \Omega_z &\approx \Omega_\parallel (-1)^{n+m}. \end{aligned} \tag{28}$$

Thus for odd (even) values of $n + m$ the angle ϕ rotates clockwise (anti-clockwise) around the singularities of the vector potential positioned at $x' = x'_{n,\max}$ and $y' = y'_{n,\max}$, whereas Ω_z alternates its sign when going from even to odd values of $n + m$. This ensures a non-zero magnetic flux over the elementary cell when integrating the vector potential around its singular points in equations (23) and (24).

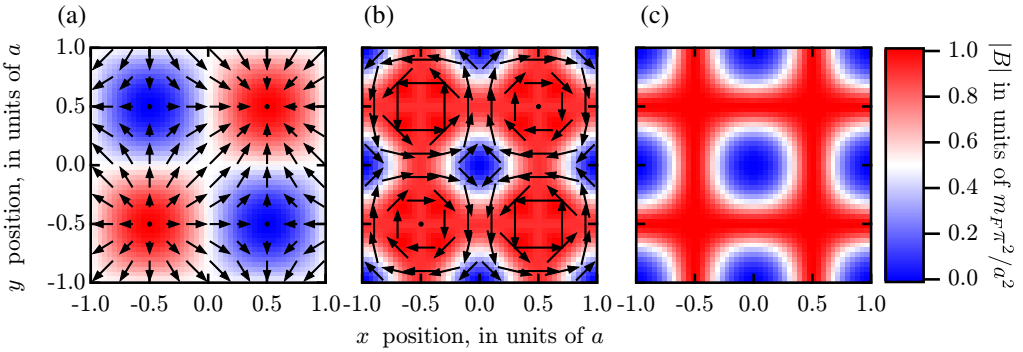

Figure 4. Rectangular coordinate flux lattice computed for $\beta = 1$. (a) Position-dependent effective Zeeman magnetic field $\mathbf{\Omega}$. The vectors denote the components in the $\mathbf{e}_x$–$\mathbf{e}_y$-plane and the color depicts the $\mathbf{e}_z$ component. (b) Geometric potentials. The color indicates the geometric scalar potential $W(\mathbf{r})$, and the arrows denote the vector potential $\boldsymbol{\mathcal{A}}(\mathbf{r})$. (c) Magnitude of effective geometric magnetic field $\boldsymbol{\mathcal{B}}$ along $\mathbf{e}_z$. Note that regions of largest $\boldsymbol{\mathcal{B}}$ correspond to the maxima of $W(\mathbf{r})$ indicated in red.

4.1. Magnetic flux

Consider now the flux passing through the elementary cell with $x' \in [0, 2\pi)$ and $y' \in [0, 2\pi)$. The vector potential $\boldsymbol{\mathcal{A}}$ has Dirac-string singularities for $\Omega_z = -\Omega_\parallel$ corresponding to odd values of $n+m$ in equation (28). Within the elementary cell these two points are positioned at $(n = 1,\ m = 0)$ and $(n = 0,\ m = 1)$, each providing $2m_F$ magnetic flux quanta. In fact, integrating the vector potential around each singular point, equations (23) and (24) yield the background magnetic flux

$$\alpha' = -\frac{1}{\hbar}\sum \oint_{\text{singul}} \boldsymbol{\mathcal{A}}\cdot \mathrm{d}\mathbf{r} = -8\pi m_F\,. \tag{29}$$

In particular, for the spin-1/2 case ($m_F = 1/2$) a measurable continuous flux over the elementary cell accommodates two Dirac quanta [48]. The same gauge-independent magnetic flux α' is obtained using the alternative vector potential $\boldsymbol{\mathcal{A}}'$ which contains gauge-dependent AB singularities at different points: $n = m = 0$ and $n = m = 1$, again each carrying $2m_F$ Dirac flux quanta.

Using equation (19), one arrives at the explicit result for the magnetic flux density

$$\boldsymbol{\mathcal{B}}(\mathbf{r}) = \hbar m_F \left(\frac{\pi}{a}\right)^2 \frac{\beta\left(f_x^2 f_y^2 - 1\right)}{\left[f_x^2 + f_y^2 + \beta^2 g_x^2 g_y^2\right]^{3/2}}\mathbf{e}_z, \tag{30}$$

where $f_u = \cos(u')$, $g_u = \sin(u')$ and $\beta = \Omega_\parallel/\Omega_\perp$. Equation (30) explicitly demonstrates that the magnetic flux, while non-uniform, is non-staggered, and its profile can be tailored by changing the ratio of the Rabi frequency amplitudes β. It is evident that the magnetic flux is zero at the potential minima $x_n = na$ and $y_m = ma$ for finite values of β. For $\beta = 1$, equation (30) is equivalent to a result obtained independently by Dalibard [59].

Figure 4 displays the spatial distribution of the effective Zeeman field $\mathbf{\Omega}$, the geometric vector and scalar potentials $\boldsymbol{\mathcal{A}}$ and W, as well as the geometric magnetic field for $\beta = 1$. Figure 5

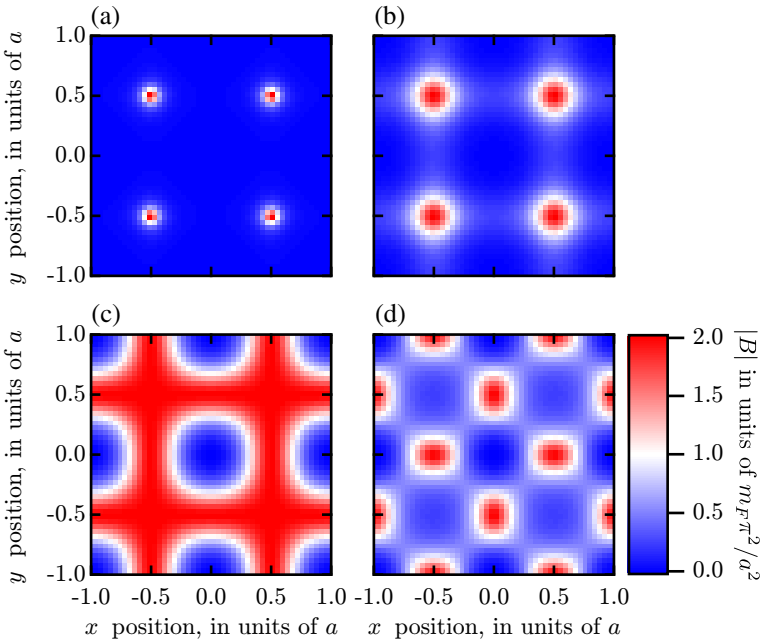

Figure 5. Dependence of geometric gauge field $\boldsymbol{\mathcal{B}}(\mathbf{r})$ on β. (a) $\beta = 0.2$, (b) $\beta = 0.5$, (c) $\beta = 1.0$ and (d) $\beta = 2.0$.

presents the geometric magnetic field $\boldsymbol{\mathcal{B}}$ for various values of β, showing that the most uniform magnetic field is reached for $\beta = 1$.

4.2. Scalar potential

Assuming that $\Omega_{\parallel} = \Omega_{\perp}$, the second term entering the scalar potential (equation (15)) is

$$\sin^2\theta\,(\nabla\phi)^2 = \left(\frac{\pi}{a}\right)^2 \frac{f_x^2 + f_y^2 - 2f_x^2 f_y^2}{\left(1 + f_x^2 f_y^2\right)\left(f_x^2 + f_y^2\right)}. \tag{31}$$

It is evident that $\sin^2\theta\,(\nabla\phi)^2$ is zero at the minima of the adiabatic energy $x_n = na$ and $y_m = ma$. Additionally, it equals $(\pi/a)^2$ at the maxima of the adiabatic energy $x_{n,\max} = na + a/2$ and $y_{m,\max} = ma + a/2$. This part of the scalar potential behaves similar to the adiabatic energy $E_-(x, y)$, thus increasing the energy maxima by $\hbar^2\pi^2/8ma^2$.

The first term entering the scalar potential (equation (15)) is

$$(\nabla\theta)^2 = \left(\frac{\pi}{a}\right)^2 \frac{g_x^2 f_y^2 (1 + f_x^2)^2 + g_y^2 f_x^2 (1 + f_y^2)^2}{\left(1 + f_x^2 f_y^2\right)\left(f_x^2 + f_y^2\right)}. \tag{32}$$

The gradient $(\nabla\theta)^2$ is zero at the minima of the adiabatic energy where $g_x = g_y = 0$, but is equal to $(\pi/a)^2$ if $f_x = f_y = 0$, i.e. at the center of each plaquette thus raising the potential there.

In this way, the geometric scalar potential is given by equation (15) together with equations (31) and (32). It is zero at the corners of a plaquette and reaches its maximum values at the center of the plaquette, thus behaving similar to the effective magnetic field, as is evident in figure 4. The scalar potential thus repels atoms from the area of high magnetic field at the center of the plaquette.

5. Alkali atoms and light shifts

In this section, we shall first demonstrate a possible way to engineer the state-independent potential $U(\mathbf{r})$ together with the state-dependent potential $\hat{M}$ featured in the general atomic Hamiltonian given by equation (1). Subsequently, we analyze atom–light configurations providing the square optical flux lattices.

Let us consider a system of ultracold alkali atoms in their electronic ground state manifold illuminated by one or several laser fields which non-resonantly couple the ground states with the lowest electronic excited states. In the presence of an external magnetic field (but without including the contributions from the laser fields), the Hamiltonian for the atomic ground state manifold is

$$H_0 = H_{\mathrm{k}} + A_{\mathrm{hf}}\hat{\mathbf{I}}\cdot\hat{\mathbf{J}} + \frac{\mu_{\mathrm{B}}}{\hbar}\mathbf{B}\cdot\left(g_J\hat{\mathbf{J}} + g_I\hat{\mathbf{I}}\right),$$

where $H_{\mathrm{k}} = \mathbf{p}^2/2m$ is the kinetic contribution to the Hamiltonian; A_{hf} is the magnetic dipole hyperfine coefficient; and μ_{B} is the Bohr magneton. The Zeeman term includes separate contributions from $\hat{\mathbf{J}} = \hat{\mathbf{L}} + \hat{\mathbf{S}}$ (the sum of the orbital $\hat{\mathbf{L}}$ and electronic spin $\hat{\mathbf{S}}$ angular momentum) and the nuclear angular momentum $\hat{\mathbf{I}}$, along with their respective Landé g-factors. We next consider the additional contributions to the atomic Hamiltonian resulting from off-resonant interaction with laser fields.

As was observed in [60–62], conventional spin-independent (scalar, U_{s}) optical potentials acquire additional spin-dependent terms near atomic resonance: the rank-1 (vector, U_{v}) and rank-2 tensor light shifts [60]. For the alkali atoms, adiabatic elimination of the excited states labeled by $j = 1/2$ (D1) and $j = 3/2$ (D2) yields an effective atom–light coupling Hamiltonian for the ground state atoms (with $j = 1/2$):

$$H_L = \left[u_{\mathrm{s}}(\mathbf{E}^*\cdot\mathbf{E}) + \frac{\mathrm{i}\,u_{\mathrm{v}}(\mathbf{E}^*\times\mathbf{E})}{\hbar}\cdot\mathbf{J}\right].$$

The rank-2 term is negligible for the parameters of interest and hence is not included in H_L. Here $\mathbf{E}$ is the optical electric field; $u_{\mathrm{v}} = -2u_{\mathrm{s}}\Delta_{\mathrm{FS}}/3(\omega-\omega_0)$ determines the vector light shift; $\Delta_{\mathrm{FS}} = \omega_{3/2} - \omega_{1/2}$ is the fine-structure splitting; $\hbar\omega_{1/2}$ and $\hbar\omega_{3/2}$ are the D1 and D2 transition energies respectively, and $\omega_0 = (2\omega_{1/2} + \omega_{3/2})/3$ is a suitable average. u_{s} sets the scale of the light shift and proportional to the atoms' ac polarizability.

The contributions from the scalar and vector light shifts featured in H_{L} can be independently specified with informed choices of laser frequency ω and intensity. Evidently, the vector light shift is a contribution to the total Hamiltonian acting as an effective magnetic field

$$\mathbf{B}_{\mathrm{eff}} = \frac{\mathrm{i}\,u_{\mathrm{v}}(\mathbf{E}^*\times\mathbf{E})}{\mu_{\mathrm{B}}g_J},$$

which acts on $\hat{\mathbf{J}}$ and not on the nuclear spin $\hat{\mathbf{I}}$. Instead of using the full Breit–Rabi equation [63] for the Zeeman energies, we assume that the Zeeman shifts are small in comparison with the hyperfine splitting—the linear, or anomalous, Zeeman regime—in which case the effective Hamiltonian for a single manifold of total angular momentum $\hat{\mathbf{F}} = \hat{\mathbf{J}} + \hat{\mathbf{I}}$ states is

$$H_0 + H_L = u_{\mathrm{s}}(\mathbf{E}^*\cdot\mathbf{E}) + \frac{\mu_{\mathrm{B}}g_F}{\hbar}(\mathbf{B}+\mathbf{B}_{\mathrm{eff}})\cdot\hat{\mathbf{F}} + \frac{A_{\mathrm{hf}}}{2}\left(\hat{\mathbf{F}}^2 - \hat{\mathbf{J}}^2 - \hat{\mathbf{I}}^2\right).$$

Note that $\mathbf{B}_{\rm eff}$ acts as a true magnetic field and adds vectorially with $\mathbf{B}$, and since $|g_I/g_J| \simeq 0.0005$ in the alkali atoms, we safely neglected a contribution $-\mu_{\rm B} g_I \mathbf{B}_{\rm eff}\cdot\hat{\mathbf{I}}/\hbar$ to the atomic Hamiltonian. We also introduced the hyperfine Landé g-factor

$$g_F = g_J \frac{f(f+1) - i(i+1) + j(j+1)}{2f(f+1)}.$$

In ^{87}Rb's lowest energy manifold with $f=1$, for which $j=1/2$ and $i=3/2$, we obtain $g_F = -g_J/4 \approx -1/2$. In the following, we always consider a single angular momentum manifold labeled by f, and select its energy at zero field as the zero of energy.

5.1. Bichromatic light field

By combining state-dependent optical lattices along with 'Raman coupling lattices', it is possible to create lattice potentials with large, non-staggered, artificial magnetic fields [48] even for alkali atoms [54]. Consider an ensemble of ultra-cold atoms subjected to a magnetic field $\mathbf{B} = B_0\mathbf{e}_z$. The atoms are illuminated by several lasers with frequencies ω and $\omega+\delta\omega$, where $\delta\omega \approx |g_F\mu_{\rm B}B_0/\hbar|$ differs by a small detuning $\delta = g_F\mu_{\rm B}B_0/\hbar - \delta\omega$ from the linear Zeeman shift between m_F states (where $|\delta| \ll \delta\omega$). In this case, the complex electric field $\mathbf{E} = \mathbf{E}_{\omega_-}\exp(-{\rm i}\,\omega t) + \mathbf{E}_{\omega_+}\exp[-{\rm i}(\omega+\delta\omega)t]$ contributes to the combined magnetic field, giving

$$\mathbf{B} + \mathbf{B}_{\rm eff} = B_0\mathbf{e}_z + \frac{{\rm i}u_{\rm v}}{\mu_{\rm B}g_J}\left[\left(\mathbf{E}^*_{\omega_-}\times\mathbf{E}_{\omega_-}\right) + \left(\mathbf{E}^*_{\omega_+}\times\mathbf{E}_{\omega_+}\right) + \left(\mathbf{E}^*_{\omega_-}\times\mathbf{E}_{\omega_+}\right){\rm e}^{-{\rm i}\delta\omega t} + \left(\mathbf{E}^*_{\omega_+}\times\mathbf{E}_{\omega_-}\right){\rm e}^{{\rm i}\delta\omega t}\right].$$

The first two terms of $\mathbf{B}_{\rm eff}$ add to the static bias field $B_0\mathbf{e}_z$, and the remaining two time-dependent terms describe transitions between different m_F levels. Provided that $B_0 \gg |\mathbf{B}_{\rm eff}|$ and $\delta\omega$ are large compared to the kinetic energy scales, the Hamiltonian can be simplified by time-averaging to zero the time-dependent terms in the scalar light shift and making the rotating wave approximation (RWA) to eliminate the time-dependence of the coupling fields. The resulting contribution to the Hamiltonian

$$\hat{H}_{\rm RWA} = U(\mathbf{r})\hat{1} + \boldsymbol{\Omega}\cdot\hat{\mathbf{F}} \tag{33}$$

takes the form of equation (1) once we identify the scalar potential

$$U(\mathbf{r}) = u_{\rm s}\left(\mathbf{E}^*_{\omega_-}\cdot\mathbf{E}_{\omega_-} + \mathbf{E}^*_{\omega_+}\cdot\mathbf{E}_{\omega_+}\right), \tag{34}$$

and the RWA effective magnetic field

$$\boldsymbol{\Omega} = \left[\delta + {\rm i}\frac{u_{\rm v}}{\hbar}\left(\mathbf{E}^*_{\omega_-}\times\mathbf{E}_{\omega_-} + \mathbf{E}^*_{\omega_+}\times\mathbf{E}_{\omega_+}\right)\cdot\mathbf{e}_z\right]\mathbf{e}_z - \frac{u_{\rm v}}{\hbar}{\rm Im}\left[\left(\mathbf{E}^*_{\omega_-}\times\mathbf{E}_{\omega_+}\right)\cdot\left(\mathbf{e}_x - {\rm i}\,\mathbf{e}_y\right)\right]\mathbf{e}_x \tag{35}$$
$$-\frac{u_{\rm v}}{\hbar}{\rm Re}\left[\left(\mathbf{E}^*_{\omega_-}\times\mathbf{E}_{\omega_+}\right)\cdot\left(\mathbf{e}_x - {\rm i}\,\mathbf{e}_y\right)\right]\mathbf{e}_y.$$

This expression is valid for $g_F > 0$ (for $g_F < 0$ the sign of the $\mathbf{e}_x$ and ${\rm i}\,\mathbf{e}_y$ terms would both be positive, owing to selecting the opposite complex terms in the RWA). The final form of this effective coupling shows that, while it is related to the initial vector light shifts, $\boldsymbol{\Omega}$ is composed of both static and resonant couplings in a way that goes beyond the restrictive $\mathbf{B}_{\rm eff} \propto {\rm i}\,\mathbf{E}^*\times\mathbf{E}$ form. This enables flux lattices in the alkali atoms.

Importantly for practical flux-lattice configurations, Ω_z depends both on the static magnetic field and on the component of $\mathbf{B}_{\rm eff}$ along $\mathbf{e}_z$. For practical considerations it is undesirable that the resonance condition be a function of the laser intensity, so we seek solutions without a contribution from this term.

5.1.1. Two Raman beams. First consider the straightforward example of the two counterpropagating Raman beams used in existing experiments [45, 46, 64–67]. In this simple case

$$\mathbf{E}_{\omega_-} = E\mathrm{e}^{\mathrm{i}k_{\mathrm{R}}x}\mathbf{e}_y \quad \text{and} \quad \mathbf{E}_{\omega_+} = E\mathrm{e}^{-\mathrm{i}k_{\mathrm{R}}x}\mathbf{e}_z,$$

describing the electric field of two lasers counterpropagating along $\mathbf{e}_x$ with equal intensities and crossed linear polarization, where $k_{\mathrm{R}} = 2\pi/\lambda$ is the single photon recoil wave vector, and $E_{\mathrm{R}} = \hbar^2 k_{\mathrm{R}}^2/2m$ is the associated recoil energy. The resulting scalar light shift $U(\mathbf{r})$ and the effective magnetic field $\mathbf{\Omega}$ describing the vector light shift are

$$U(\mathbf{r}) = u_{\mathrm{s}}\left(\mathbf{E}^*_{\omega_-}\cdot\mathbf{E}_{\omega_-} + \mathbf{E}^*_{\omega_+}\cdot\mathbf{E}_{\omega_+}\right) = 2u_{\mathrm{s}}E^2$$

$$\mathbf{\Omega} = \delta\mathbf{e}_z + \Omega_{\mathrm{R}}\left[\sin\left(2k_{\mathrm{R}}x\right)\mathbf{e}_x - \cos\left(2k_{\mathrm{R}}x\right)\mathbf{e}_y\right],$$

where $\Omega_{\mathrm{R}} = u_{\mathrm{v}}E^2/\hbar$. These describe a constant scalar light shift along with a spatially rotating effective magnetic field, as discussed in [64] which produced an artificial spin–orbit coupling, and in different notation, is equivalent to the proposal of [40]. Because this Hamiltonian is only invariant under spatial translations with primitive vector $\mathbf{u} = \pi/k_{\mathrm{R}}\mathbf{e}_x$, it would be expected to describe a periodic lattice. However, transforming the complete Hamiltonian according to the rotation $\hat{U}(x)\hat{H}\hat{U}^\dagger(x)$, with $\hat{U}(x) = \exp[\mathrm{i}\,\hat{F}_z(2k_{\mathrm{R}}x - \pi/2)/\hbar]$, completely removes the spatial periodicity. Instead, the transformed Hamiltonian becomes

$$\hat{H} = \frac{\hbar^2}{2m}\left(\hat{k} - 2k_{\mathrm{R}}\hat{F}_z/\hbar\right)^2 + U(\mathbf{r})\hat{1} + \delta\hat{F}_z + \Omega_{\mathrm{R}}\hat{F}_x,$$

in which the position dependence has vanished from coupling vector $\delta\mathbf{e}_z + \Omega_{\mathrm{R}}\mathbf{e}_y$. In this example, all spatial dependence (including the initial lattice structure) has been eliminated from the Hamiltonian in exchange for a matrix-valued (although Abelian) gauge field. An additional spatially uniform radio-frequency magnetic field added to the mix forces the spatial structure to remain, creating a composite lattice potential [68].

5.1.2. Flux-lattice configuration. Next, we analyze the configuration shown in figure 6 where four beams with angular frequency ω intersecting at right angles in the $\mathbf{e}_x$–$\mathbf{e}_y$-plane are joined by a fifth beam with angular frequency $\omega + \delta\omega$ traveling along $\mathbf{e}_z$. The total electric field from these five beams is

$$\mathbf{E}_{\omega_-} = \mathbf{E}_{x^+} + \mathbf{E}_{x^-} + \mathbf{E}_{y^+} + \mathbf{E}_{y^-} \quad \text{and} \quad \mathbf{E}_{\omega_+} = \mathbf{E}_z,$$

where

$$\begin{aligned}
\mathbf{E}_{x^+} &= E_{xy}\left(\mathrm{e}^{-\mathrm{i}\phi/2}\cos\theta_p\mathbf{e}_z + \mathrm{e}^{\mathrm{i}\phi/2}\sin\theta_p\mathbf{e}_y\right)\mathrm{e}^{\mathrm{i}\delta\phi_x/2}\mathrm{e}^{\mathrm{i}\delta\phi_{xy}/2}\mathrm{e}^{\mathrm{i}k_{\mathrm{R}}x},\\
\mathbf{E}_{x^-} &= E_{xy}\left(\mathrm{e}^{-\mathrm{i}\phi/2}\cos\theta_p\mathbf{e}_z - \mathrm{e}^{\mathrm{i}\phi/2}\sin\theta_p\mathbf{e}_y\right)\mathrm{e}^{-\mathrm{i}\delta\phi_x/2}\mathrm{e}^{\mathrm{i}\delta\phi_{xy}/2}\mathrm{e}^{-\mathrm{i}k_{\mathrm{R}}x},\\
\mathbf{E}_{y^+} &= E_{xy}\left(\mathrm{e}^{\mathrm{i}\phi/2}\cos\theta_p\mathbf{e}_z - \mathrm{e}^{-\mathrm{i}\phi/2}\sin\theta_p\mathbf{e}_x\right)\mathrm{e}^{\mathrm{i}\delta\phi_y/2}\mathrm{e}^{-\mathrm{i}\delta\phi_{xy}/2}\mathrm{e}^{\mathrm{i}k_{\mathrm{R}}y},\\
\mathbf{E}_{y^-} &= E_{xy}\left(\mathrm{e}^{\mathrm{i}\phi/2}\cos\theta_p\mathbf{e}_z + \mathrm{e}^{-\mathrm{i}\phi/2}\sin\theta_p\mathbf{e}_x\right)\mathrm{e}^{-\mathrm{i}\delta\phi_y/2}\mathrm{e}^{-\mathrm{i}\delta\phi_{xy}/2}\mathrm{e}^{-\mathrm{i}k_{\mathrm{R}}y},\\
\mathbf{E}_z &= \frac{E_z}{\sqrt{2}}\left(\mathbf{e}_x + \mathbf{e}_y\right)\mathrm{e}^{\mathrm{i}k_{\mathrm{R}}z}.
\end{aligned}$$

In this complicated set of fields, ϕ describes the ellipticity of the lasers traveling in the $\mathbf{e}_x$–$\mathbf{e}_y$-plane, the major axes of which are tipped by an angle θ_p from vertical. When $\phi = \pi/2$ all four beams are right-hand circular polarized. $\delta\phi_x$ and $\delta\phi_y$ describe relative phase differences

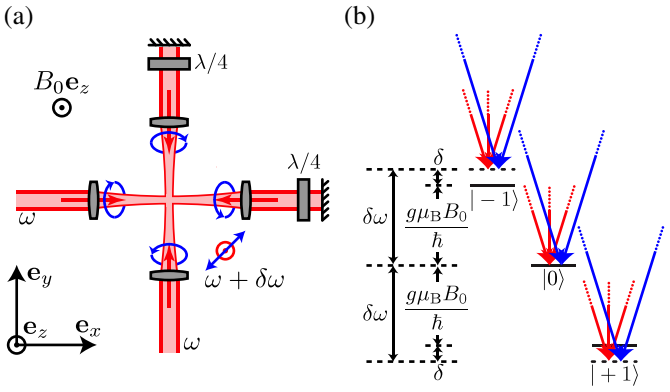

Figure 6. Proposed experimental geometry. (a) Laser geometry for creating flux lattice showing the four circularly polarized beams in the $\mathbf{e}_x$–$\mathbf{e}_y$-plane with frequency ω along with the linearly polarized beam traveling along $\mathbf{e}_z$ with frequency $\omega + \delta\omega$. (b) Physical level diagram for the three-level total angular momentum $f = 1$ case with m_F states labeled, as is applicable for the common alkali atoms ^{7}Li, ^{23}Na, ^{39}K, ^{41}K and ^{87}Rb. For reference, the diagram shows the decomposition of these optical fields into $\sigma_\pm$ and π, but as discussed in the text, this is not an overly useful way of considering this problem. The red beams have frequency ω and the blue beams have frequency $\omega + \delta\omega$.

between the forward- and counter-propagating beams along $\mathbf{e}_x$ and $\mathbf{e}_y$, respectively; lastly, $\delta\phi_{xy}$ is an overall phase difference between the beams traveling along $\mathbf{e}_x$ and those traveling along $\mathbf{e}_y$ (a similar phase difference $\delta\phi_z$ exists between the $\mathbf{e}_x$–$\mathbf{e}_y$ beams and the $\mathbf{e}_z$ beam; however, it amounts to simply displacing the system along $\mathbf{e}_z$).

For this set of fields, the scalar light shift (neglecting a $u_s(4E_{xy}^2 + E_z^2)$ energy offset) is

$$U(\mathbf{r}) = U_\perp \left[\cos(2x') + \cos(2y')\right] + U_\parallel \cos x' \cos y', \tag{36}$$

where we have introduced the scalar energies $U_\perp = 2u_s E_{xy}^2 \cos\left(2\theta_p\right)$ and $U_\parallel = 8u_s E_{xy}^2 \cos^2\theta_p \cos(2\varphi_-)$, with $\varphi_\pm = (\delta\phi_{xy} \pm \phi)/2$. The RWA effective magnetic field becomes

$$\begin{aligned}\mathbf{\Omega} = \Omega_\perp &\left[\cos\left(x'\right)\sin\left(z' - \varphi_-\right) + \cos\left(y'\right)\sin\left(z' + \varphi_-\right)\right]\mathbf{e}_x + \Omega_\perp\left[\cos\left(x'\right)\cos\left(z' - \varphi_-\right)\right. \\ &\left. + \cos\left(y'\right)\cos\left(z' + \varphi_-\right)\right]\mathbf{e}_y + \Omega_\parallel\left[\sin(x')\sin(y') + \tilde{\delta}\right]\mathbf{e}_z.\end{aligned} \tag{37}$$

We defined $\Omega_\perp = 2u_v E_{xy} E_z \cos\theta_p/\hbar$ and $\Omega_\parallel = 4u_v E_{xy}^2 \sin(2\varphi_+)\sin^2\theta_p/\hbar$ and introduced a dimensionless detuning $\tilde{\delta} = \delta/\hbar\Omega_\parallel$. (Here, $\mathbf{E}_z$ is linearly polarized, so it does not have any contributions to δ, as would be the case for a circularly polarized beam [48].) In these expressions, we made the simplifying replacements $x' = k_R x - \delta\phi_x/2$, $y' = k_R y - \delta\phi_y/2$ and $z' = k_R z + \pi/4$. These show that the phase-differences between beams traveling along $\mathbf{e}_x$ and $\mathbf{e}_y$ give rise only to effective spatial displacements leaving the topology of the lattice unchanged; in contrast, the phase difference between the $\mathbf{e}_x$ and $\mathbf{e}_y$ lasers $\delta\phi_{xy}$ fundamentally changes the coupling.

Somewhat more subtly, transforming the complete Hamiltonian according to the unitary rotation $\hat{U}(x)\hat{H}\hat{U}^\dagger(x)$, with $\hat{U}(x) = \exp(\mathrm{i}\,\hat{F}_z z'/\hbar)$ completely eliminates the z-dependence

from the Hamiltonian, but as in section 5.1.1, introduces a gauge field $k_L \hat{F}_z$ for motion along $\mathbf{e}_z$. Under this transformation the effective Zeeman term becomes

$$\hat{U}(x)\left[\hat{\mathbf{F}}\cdot\boldsymbol{\Omega}(z')\right]\hat{U}^{\dagger}(x) = \hat{\mathbf{F}}\cdot\boldsymbol{\Omega}(z'=0).$$

Therefore the Hamiltonian separates into a sum of independent contributions for motion along $\mathbf{e}_z$ and motion in the $\mathbf{e}_x$–$\mathbf{e}_y$-plane; without loss of generality, we take $z' = \pi/4$. The expression for $\boldsymbol{\Omega}$ then reduces to that of equation (25) for the physical parameters $\phi = \pi/2$ (circularly polarized beams in the $\mathbf{e}_x$–$\mathbf{e}_y$-plane), $\phi_{xy} = 0$ and $\tilde{\delta} = 0$.

With the replacement $\beta = \Omega_{\parallel}/\Omega_{\perp}$, the resulting adiabatic orbital field is

$$\boldsymbol{\mathcal{B}}(\mathbf{r}) = \hbar m_f \left(\frac{\pi}{a}\right)^2 \frac{\beta\left(f_x^2 f_y^2 - 1 - \tilde{\delta} g_x g_y\right)\sin(-2\varphi_-)}{\left[f_x^2 + f_y^2 + 2 f_x f_y \cos(2\varphi_-) + \beta^2\left(\tilde{\delta} + g_x g_y\right)^2\right]^{3/2}}\mathbf{e}_z. \tag{38}$$

This implies that practical implementations of flux lattices require active stabilization of the phase between beams traveling along $\mathbf{e}_x$ and $\mathbf{e}_y$, but not the $\mathbf{e}_z$ beam. For the choice $\varphi_- = -\pi/4$ and $\tilde{\delta} = 0$ this reduces to equation (30).

Given the dependence of $\boldsymbol{\mathcal{B}}(\mathbf{r})$ on so many parameters, we now consider the first order sensitivity to perturbations in $\tilde{\delta} = \Delta\tilde{\delta}$ and $\varphi_- = -\pi/4 + \Delta\varphi_-$; since changes in phase sum $\varphi_+ = \pi/4 + \Delta\varphi_0$ enter into $\Omega_{\parallel}$ quadratically, they may be neglected at first order. Additionally, the polarization angle θ_{P} is generally static in the laboratory, and an imperfect setting can be accounted for by changing the intensity of the Raman beams. We find the scalar light shift is unchanged, but the effective coupling becomes

$$\begin{aligned}\Omega = {} & \Omega_{\perp}\left[\cos\left(x'\right) + \Delta\varphi_- \cos\left(y'\right)\right]\mathbf{e}_x + \Omega_{\perp}\left[-\Delta\varphi_- \cos\left(x'\right) + \cos\left(y'\right)\right]\mathbf{e}_y \\ & + \Omega_{\parallel}\left[\sin(x')\sin(y') + \Delta\tilde{\delta}\right]\mathbf{e}_z.\end{aligned} \tag{39}$$

Given this, it is surprising but delightful that we arrive at an orbital field which is unaltered at first order. We observe that $\Delta\tilde{\delta}$ usually results from noise in the magnetic field; here this noise must be small compared to the coupling strength $\Omega_{\parallel}$, not the generally much smaller width of the Bloch bands.

5.2. Band structure and Chern numbers

The adiabatic arguments show that flux lattices give rise to large orbital magnetic fields with non-zero average. As we learned above, the spatial locations with largest magnetic field are also associated with a repulsive adiabatic scalar potential $W(\mathbf{r})$, suggesting that without a compensating term from the scalar potential $U(\mathbf{r})$ the magnetic field might not be important for atoms in the lowest bands. To address this question, we studied the resulting band structure and identified when the Bloch bands have a non-zero Chern number, in analogy with the band structure of charged particles in a magnetic field. We directly compute the band structure from potential terms in equation (33) combined with the contribution from the usual kinetic energy term and then extract the Chern numbers using the prescription in [69].

The Hamiltonian described by equation (33) has apparent primitive lattice vectors $\mathbf{u}_1 = 2\pi/k_{\mathrm{R}}\mathbf{e}_x$ and $\mathbf{u}_2 = 2\pi/k_{\mathrm{R}}\mathbf{e}_y$ (each of these is twice as large as usual for a lattice formed by

retro-reflected lasers). To compute the band structure in the simplest manner, we first rotated the coordinate system in equations (36) and (37) by $\pi/4$ in the $\mathbf{e}_x$–$\mathbf{e}_y$-plane and defined scaled coordinates $x'' = y' + x'$ and $y'' = y' - x'$. In analogy with the procedure described in section 5.1.1, we applied a spatially dependent rotation

There should be a k_R in the numerator on the first expression in the exponent.

$$U(\mathbf{r}) = \exp\left[\frac{\mathrm{i}\,(x'' + y'')\,\hat{F}_z}{2\hbar}\right] = \exp\left[\frac{\mathrm{i}\,k_\mathrm{R}\,y\,\hat{F}_z}{\hbar}\right],$$

which introduced a gauge term in the kinetic energy. In the example given in section 5.1.1, this process completely removed the Hamiltonian's spatial dependence; here it does not, but the area of the unit cell is halved (the primitive lattice vectors $\mathbf{u}_1 = \pi/2k_\mathrm{R}(\mathbf{e}_x + \mathbf{e}_y)$ and $\mathbf{u}_2 = \pi/2k_\mathrm{R}(-\mathbf{e}_x + \mathbf{e}_y)$ expressed in the initial coordinate system are reduced in magnitude by a factor of $1/\sqrt{2}$), doubling the area of the Brillouin zone [48]. The resulting Hamiltonian has contributions

In this equation k_L should be k_R. This introduces a sqrt(2) difference. There should also be a hbar in the denominator

$$\begin{aligned} H_k &= \frac{\hbar^2}{2m}\left[\left(k_x - k_\mathrm{L}\hat{F}_z/2\right)^2 + \left(k_y - k_\mathrm{L}\hat{F}_z/2\right)^2\right] \\ U(\mathbf{r}) &= U_\perp\left[\cos(x'' + y'') + \cos(x'' - y'')\right] + \frac{U_\parallel}{2}\left[\cos\left(x''\right) + \cos\left(y''\right)\right] \\ \hat{\mathbf{F}}\cdot\boldsymbol{\Omega} &= \hat{F}_z\Omega_z + \hat{F}_+\Omega_- + \hat{F}_-\Omega_+, \end{aligned} \tag{40}$$

where $\hat{F}_\pm = \hat{F}_x \pm \mathrm{i}\hat{F}_y$ are the usual angular momentum raising and lower operators; the coupling expressed in the helicity basis is quite simple with

$$\Omega_z = \frac{\Omega_\parallel}{2}\left[-\cos(x'') + \cos(y'') + \tilde{\delta}\right],$$

$$\Omega_+ = \Omega_-^\dagger = \frac{\mathrm{i}\,\Omega_\perp}{4}\left[\mathrm{e}^{\mathrm{i}(x''+\varphi_-)} + \mathrm{e}^{\mathrm{i}(y''+\varphi_-)} + \mathrm{e}^{\mathrm{i}(x''+y''-\varphi_-)} + \mathrm{e}^{-\mathrm{i}\varphi_-}\right].$$

All these expressions fully respect translational symmetry in the reduced unit cell whose reciprocal lattice vectors have magnitude $k_\mathrm{L} = \sqrt{2}k_\mathrm{R}$, and a recoil energy $E_\mathrm{L} = 2E_\mathrm{R}$. From this, computation of the band structure and its Chern numbers is straightforward.

Figure 7 depicts the outcome of this computation for an optimally chosen parameter set (values given in the caption). While the Chern number of the lowest band C_0 is non-zero over a wide range of parameters, the red contours illustrate the most significant limitation for practical implementation of these flux lattices: the relatively small gap between the ground and first excited bands ΔE_{01}. For our optimal parameter set, we find a maximal gap of just $\Delta E_{01} = 0.107E_\mathrm{L} = 0.214E_\mathrm{R}$, far less than the $U \approx 1E_\mathrm{R}$ on-site interaction energy in typical 3D optical lattices (a slight improvement is possible by tuning the quadratic Zeeman term which was absent in these computations). This implies that interactions will hybridize several of the lowest bands in a way that cannot be described as a perturbation of the lowest band as is possible in conventional optical lattices where $\Delta E_{01} \gtrsim 10E_\mathrm{L}$. Moreover, the geometric magnetic field through each unit cell always has m_F quanta of flux, leading to the misguided intuitive expectation of high magnetic field physics everywhere. Instead, the competing localization from the strong lattice potential restricts the topological non-trivial band structure to a modest parameter range.

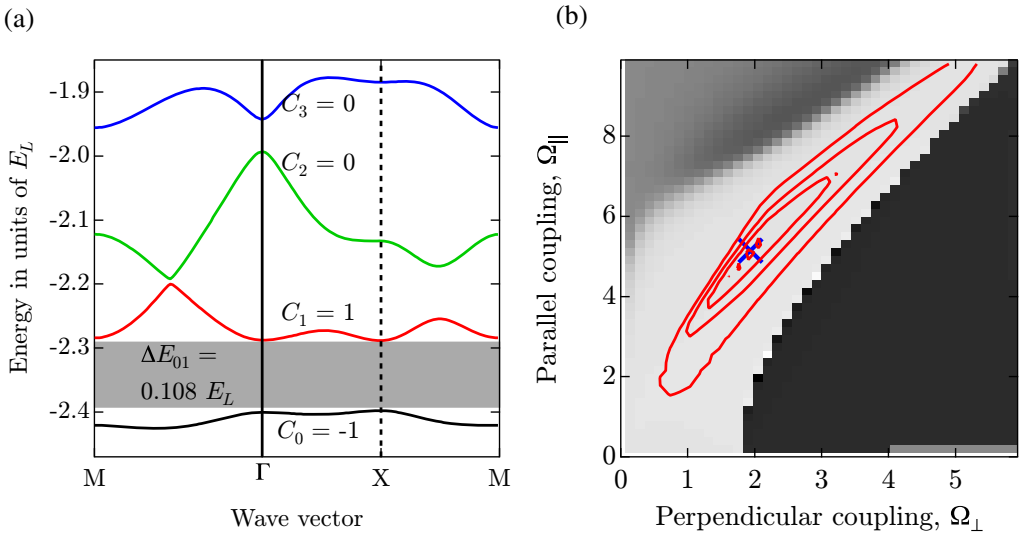

Figure 7. Band structure. (a) Band structure for the lowest four bands showing the Chern numbers C_n, and the modest energy gap ΔE_{01} between the ground and first excited bands. These were computed for $\Omega_\perp = 1.905E_\mathrm{L}$, $\Omega_\parallel = 5.1E_\mathrm{L}$, $U_\perp = -1.95E_\mathrm{L}$, $U_\parallel = 0$, $\delta = 0$ and the phase $\phi_- = -\pi/4$. (b) Ground band Chern number as a function of $\Omega_\perp$ and $\Omega_\parallel$ for the same $U_\perp$ and $U_\parallel$ as above. White indicates a Chern number $C_n = -1$, and black indicates $C_n = 0$; the gray region is where two bands touch and neither have integer C_n (although the sum is of course quantized). The red contours mark ΔE_{01} in this plane, showing the modest parameter region where it is non-negligible, and the blue cross locates the maximum gap of $\Delta E_{01} = 0.107E_\mathrm{L}$ where the band structure of (a) was computed. The contours (from outside to inside) correspond to $\Delta E_{01}/E_\mathrm{L} = \{0.025, 0.05, 0.075, 0.1\}$.

6. Concluding remarks

We have explored the optical flux lattices produced for ultra-cold atoms in the radiation field when both the atom–light coupling and the detuning exhibit an oscillatory behavior. We have analyzed not only the magnetic flux but also the geometric vector potential generating the flux, as well as the accompanying geometric scalar potential. We showed how to deal with the gauge-dependent singularities of the AB type appearing in the vector potentials for the optical flux lattices. We have presented a way to calculate the continuous magnetic flux through the elementary cell via the singularities of the vector potential inside the cell. The analysis is illustrated with a square optical flux lattice. We have presented a way of creating such a lattice using the Raman transitions induced by a set of properly chosen polarization-dependent standing waves propagating at a right angle and containing a time-phase difference.

Acknowledgments

We acknowledge helpful discussions with Jean Dalibard, Nigel Cooper, Tilman Esslinger, Janne Ruostekoski, Julius Ruseckas, Algirdas Mekys and Simonas Grubinskas. In addition,

we appreciate a careful reading by L J LeBlanc. GJ acknowledges support from the Research Council of Lithuania (grant no. MIP-082/2012). IBS acknowledges financial support from the NSF through the PFC at JQI, and the ARO through funds from both the Atomtronics MURI and the DARPA OLE Program.

References

[1] Lewenstein M, Sanpera A, Ahufinger V, Damski B, De Sen A and Sen U 2007 Ultracold atomic gases in optical lattices: mimicking condensed matter physics and beyond *Adv. Phys.* **56** 243–379
[2] Ketterle W and Zwierlein M 2007 *Ultra Cold Fermi Gases (Proc. Int. School of Physics 'Enrico Fermi' vol CLXIV)* ed M Inguscio, W Ketterle and C Salomon (Amsterdam: IOS Press)
[3] Bloch I, Dalibard J and Zwerger W 2008 Many-body physics with ultracold gases *Rev. Mod. Phys.* **80** 885
[4] Giorgini S, Pitaevskii L P and Stringari S 2008 Theory of ultracold atomic Fermi gases *Rev. Mod. Phys.* **80** 1215
[5] Greiner M, Mandel O, Esslinger T, Hänsch T W and Bloch I 2002 Quantum phase transition from a superfluid to a Mott insulator in a gas of ultracold atoms *Nature* **415** 39–44
[6] Hadzibabic Z, Krüger P, Cheneau M, Battelier B and Dalibard J 2006 Berezinskii–Kosterlitz–Thouless crossover in a trapped atomic gas *Nature* **441** 1118–21
[7] Greiner M, Regal C A and Jin D S 2003 Emergence of a molecular Bose–Einstein condensate from a Fermi gas *Nature* **426** 537–40
[8] Zwierlein M, Stan C, Schunck C, Raupach S, Kerman A and Ketterle W 2004 Condensation of pairs of fermionic atoms near a Feshbach resonance *Phys. Rev. Lett.* **92** 120403
[9] von Klitzing K 1986 The quantized Hall effect *Rev. Mod. Phys.* **58** 519–31
[10] Cooper N R 2008 Rapidly rotating atomic gases *Adv. Phys.* **57** 539–616
[11] Fetter A L 2009 Rotating trapped Bose–Einstein condensates *Rev. Mod. Phys.* **81** 647
[12] Dalibard J, Gerbier F, Juzeliūnas G and Öhberg P 2011 Artificial gauge potentials for neutral atoms *Rev. Mod. Phys.* **83** 1523–43
[13] Jaksch D and Zoller P 2003 Creation of effective magnetic fields in optical lattices: the Hofstadter butterfly for cold neutral atoms *New J. Phys.* **5** 56
[14] Mueller E J 2004 Artificial electromagnetism for neutral atoms: Escher staircase and Laughlin liquids *Phys. Rev.* A **70** 041603
[15] Sørensen A S, Demler E and Lukin M D 2005 Fractional quantum Hall states of atoms in optical lattices *Phys. Rev. Lett.* **94** 086803
[16] Osterloh K, Baig M, Santos L, Zoller P and Lewenstein M 2005 Cold atoms in non-Abelian gauge potentials: from the Hofstadter 'moth' to lattice gauge theory *Phys. Rev. Lett.* **95** 010403
[17] Lim L-K, Morais Smith C and Hemmerich A 2008 Staggered-vortex superfluid of ultracold bosons in an optical lattice *Phys. Rev. Lett.* **100** 130402
[18] Gerbier F and Dalibard J 2010 Gauge fields for ultracold atoms in optical superlattices *New J. Phys.* **12** 033007
[19] Kolovsky A R 2011 Creating artificial magnetic fields for cold atoms by photon-assisted tunneling *Europhys. Lett.* **93** 20003
[20] Kitagawa T, Berg E, Rudner M and Demler E 2010 Topological characterization of periodically driven quantum systems *Phys. Rev.* B **82** 235114
[21] Aidelsburger M, Atala M, Nascimbàne S, Trotzky S, Chen Y-A and Bloch I 2011 Experimental realization of strong effective magnetic fields in an optical lattice *Phys. Rev. Lett.* **107** 255301
[22] Struck J, Ölschläger C, Weinberg M, Hauke P, Simonet J, Eckardt A, Lewenstein M, Sengstock K and Windpassinger P 2012 Tunable gauge potential for neutral and spinless particles in driven optical lattices *Phys. Rev. Lett.* **108** 225304
[23] Ruostekoski J, Dunne G V and Javanainen J 2002 Particle number fractionilization of an atomic Fermi–Dirac gas in an optical lattice *Phys. Rev. Lett.* **88** 180401

[24] Berry M V 1984 Quantal phase factors accompanying adiabatic changes *Proc. R. Soc. Lond.* A **392** 45–57
[25] Jackiw R 1988 *Comment. At. Mol. Phys.* **21** 71
[26] Moody J, Shapere A and Wilczek F 1986 Realizations of magnetic-monopole gauge fields: diatoms and spin precession *Phys. Rev. Lett.* **56** 893
[27] Bohm A, Kendrick B, Loewe M E and Boya L J 1992 The Berry connection and Born–Oppenheimer method *J. Math. Phys.* **33** 977
[28] Zee A 1988 Non-Abelian gauge structure in nuclear quadrupole resonance *Phys. Rev.* A **38** 1
[29] Shapere A and Wilczek F (ed) 1989 *Geometric Phases in Physics* (Singapore: World Scientific)
[30] Alden Mead C 1992 The geometric phase in molecular physics *Rev. Mod. Phys.* **84** 51
[31] Bohm A, Mostafazadeh A, Koizumi H, Niu Q and Zwanziger J 2003 *Geometric Phases in Quantum Systems* (Berlin: Springer)
[32] Xiao D, Chang M-C and Niu Q 2010 Berry phase effects on electronic properties *Rev. Mod. Phys.* **82** 1959
[33] Dum R and Olshanii M 1996 Gauge structures in atom-laser interaction: Bloch oscillations in a dark lattice *Phys. Rev. Lett.* **76** 1788–91
[34] Visser P M and Nienhuis G 1998 Geometric potentials for subrecoil dynamics *Phys. Rev.* A **57** 4581–91
[35] Dutta S K, Teo B K and Raithel G 1999 Tunneling dynamics and gauge potentials in optical lattices *Phys. Rev. Lett.* **83** 1934–7
[36] Juzeliūnas G and Öhberg P 2004 Slow light in degenerate Fermi gases *Phys. Rev. Lett.* **93** 033602
[37] Juzeliūnas G, Ruseckas J and Öhberg P 2005 Effective magnetic fields induced by EIT in ultra-cold atomic gases *J. Phys. B: At. Mol. Opt. Phys.* **38** 4171
[38] Ruseckas J, Juzeliūnas G, Öhberg P and Fleischhauer M 2005 Non-Abelian gauge potentials for ultracold atoms with degenerate dark states *Phys. Rev. Lett.* **95** 06
[39] Zhang P, Li Y and Sun C P 2005 Induced magnetic monopole from trapped λ-type atom *Eur. Phys. J.* D **36** 229
[40] Juzeliūnas G, Ruseckas J, Öhberg P and Fleischhauer M 2006 Light-induced effective magnetic fields for ultracold atoms in planar geometries *Phys. Rev.* A **73** 025602
[41] Zhu S-L, Fu H, Wu C-J, Zhang S-C and Duan L-M 2006 Spin Hall effects for cold atoms in a light-induced gauge potential *Phys. Rev. Lett.* **97** 240401
[42] Günter K J, Cheneau M, Yefsah T, Rath S P and Dalibard J 2009 Practical scheme for a light-induced gauge field in an atomic Bose gas *Phys. Rev.* A **79** 011604
[43] Cooper N R and Hadzibabic Z 2010 Measuring the superfluid fraction of an ultracold atomic gas *Phys. Rev. Lett.* **104** 030401
[44] Spielman I B 2009 Raman processes and effective gauge potentials *Phys. Rev.* A **79** 063613
[45] Lin Y J, Compton R L, Jimenez-Garcia K, Porto J V and Spielman I B 2009 Synthetic magnetic fields for ultracold neutral atoms *Nature* **462** 628–32
[46] Lin Y-J, Compton R L, Perry A R, Phillips W D, Porto J V and Spielman I B 2009 Bose–Einstein condensate in a uniform light-induced vector potential *Phys. Rev. Lett.* **102** 130401
[47] Laughlin R B, Stormer H L and Tsui D C 1999 Nobel lecture: the fractional quantum Hall effect *Rev. Mod. Phys.* **71** 863–95
[48] Cooper N 2011 Optical flux lattices for ultracold atomic gases *Phys. Rev. Lett.* **106** 175301
[49] Spielman I 2011 An optical lattice of flux *Physics* **4** 35
[50] Aharonov Y and Bohm D 1959 Significance of electromagnetic potentials in quantum theory *Phys. Rev.* **115** 485
[51] Peierls R 1933 *Z. Phys.* **80** 763
[52] Luttinger J M 1951 The effect of a magnetic field on electrons in a periodic potential *Phys. Rev.* **84** 814–7
[53] Hofstadter D R 1976 Energy levels and wave functions of Bloch electrons in rational and irrational magnetic fields *Phys. Rev.* B **14** 2239–49
[54] Cooper N R and Dalibard J 2011 Optical flux lattices for two-photon dressed states *Europhys. Lett.* **95** 66004
[55] Zygelman B 1987 Appearance of gauge potentials in atomic collision physics *Phys. Lett.* A **125** 476

[56] Zygelman B 1990 Non-Abelian geometric phase and long-range atomic forces *Phys. Rev. Lett.* **64** 256
[57] Aharonov Y and Stern A 1992 Origin of the geometric forces accompanying Berry's geometric potentials *Phys. Rev. Lett.* **69** 3593–7
[58] Cheneau M, Rath S P, Yefsah T, Gunter K J, Juzeliūnas G and Dalibard J 2008 Geometric potentials in quantum optics: a semi-classical interpretation *Europhys. Lett.* **83** 60001
[59] Dalibard J 2011 private communication
[60] Deutsch I H and Jessen P S 1998 Quantum-state control in optical lattices *Phys. Rev.* A **57** 1972–86
[61] Dudarev A M, Diener R B, Carusotto I and Niu Q 2004 Spin–orbit coupling and Berry phase with ultracold atoms in 2D optical lattices *Phys. Rev. Lett.* **92** 153005
[62] Sebby-Strabley J, Anderlini M, Jessen P S and Porto J V 2006 Lattice of double wells for manipulating pairs of cold atoms *Phys. Rev.* A **73** 033605
[63] Breit G and Rabi I I 1931 Measurement of nuclear spin *Phys. Rev.* **38** 2082–3
[64] Lin Y-J, Jiménez-García K and Spielman I B 2011 Spin–orbit-coupled Bose–Einstein condensates *Nature* **471** 83–6
[65] Zhang J-Y *et al* 2012 Collective dipole oscillations of a spin–orbit coupled Bose–Einstein condensate *Phys. Rev. Lett.* **109** 115301
[66] Wang P, Yu Z-Q, Fu Z, Miao J, Huang L, Chai S, Zhai H and Zhang J 2012 Spin–orbit coupled degenerate Fermi gases *Phys. Rev. Lett.* **109** 095301
[67] Cheuk L W, Sommer A T, Hadzibabic Z, Yefsah T, Bakr W S and Zwierlein M W 2012 Spin-injection spectroscopy of a spin–orbit coupled Fermi gas *Phys. Rev. Lett.* **109** 095302
[68] Jiménez-García K, LeBlanc L J, Williams R A, Beeler M C, Perry A R and Spielman I B 2012 The Peierls substitution in an engineered lattice potential *Phys. Rev. Lett.* **108** 225303
[69] Fukui T, Hatsugai Y and Suzuki H 2005 Chern numbers in discretized Brillouin zone: efficient method of computing (Spin) Hall conductances *J. Phys. Soc. Japan* **74** 1674–7